Research Article | Vol. 28, No. 26 / 21 December 2020 / *Optics Express* 39963

Optics EXPRESS

Quantum-correlated photon-pair generation via cascaded nonlinearity in an ultra-compact lithium-niobate nano-waveguide

BRADLEY S. ELKUS,[1,*] KAMAL ABDELSALAM,[2] SASAN FATHPOUR,[2,3] PREM KUMAR,[1] AND GREGORY S. KANTER[1]

[1] *Department of Electrical and Computer Engineering, Center for Photonic Communication and Computing, Northwestern University, 2145 Sheridan Road, Evanston, Illinois 60208-3118, USA*
[2] *CREOL, The College of Optics and Photonics, University of Central Florida, Orlando, Florida 32816, USA*
[3] *Department of Electrical and Computer Engineering, University of Central Florida, Orlando, Florida 32816, USA*
[*] *bradleyelkus2013@u.northwestern.edu*

Abstract: We generate quantum-correlated photon pairs using cascaded $\chi^{(2)} : \chi^{(2)}$ traveling-wave interactions for second-harmonic generation (SHG) and spontaneous parametric down-conversion (SPDC) in a single periodically-poled thin-film lithium-niobate (TFLN) waveguide. When pulse-pumped at 50 MHz, a 4-mm-long poled region with nearly 300%/Wcm^2 SHG peak efficiency yields a generated photon-pair probability of $7 \pm 0.2 \times 10^{-4}$ with corresponding coincidence-to-accidental ratio (CAR) of 13.6±0.7. The CAR is found to be limited by Stokes/anti-Stokes Raman-scattering noise generated primarily in the waveguide. A Raman peak of photon counts at 250 cm^{-1} Stokes shift from the fundamental-pump wavenumber suggests most of the noise that limits the CAR originates within the lithium niobate material of the waveguide.

1. Introduction

Thin-film lithium niobate (TFLN) integrated photonics has made great strides in the last few years for electro-optic and nonlinear-optics applications [1], while studies in the quantum domain have just started taking off. Recent progress has been made in demonstrating quantum-correlated [2,3] and entangled [4] photon-pair generation via traveling-wave SPDC in periodically-poled TFLN waveguide platforms [5]. In SPDC, a higher-energy (-frequency) pump photon spontaneously splits to simultaneously create lower-energy (-frequency) daughter photons in the signal and idler bands, a process which is essentially parametric amplification of input vacuum fluctuations in the signal/idler bands by the pump light. For this process to efficiently occur, the pump frequency is usually chosen to lie in the second-harmonic (SH) phase-matching bandwidth of the waveguide. To the best of our knowledge, traveling-wave quantum-correlated photon-pair generation in this new TFLN waveguide platform has only involved pumping a single waveguide directly by the SH field that's phase-matched with the chosen signal-idler bands [2–4]. Therefore, the pumps for photon-pair generation in the telecom C/S/L bands in these experiments have occupied the visible-to-near-infrared boundary of the optical spectrum, which is not telecom compatible. It is, however, attractive to use telecom-compatible pump wavelengths to generate correlated photon-pairs in the desirable telecom C-band, which can be realized by using two waveguides—with similar phase-matching characteristics—in series and pumping them at the SH phase-matching peak [6,7]. The first waveguide is pumped by a fundamental-pump in the telecom band for generating the SH; this SH serves as the pump for SPDC in the second waveguide.

Instead of using two separate waveguides, correlated/entangled photon-pair generation can take place in a single waveguide via a cascaded nonlinear interaction, wherein the SPDC pump and

#411575 https://doi.org/10.1364/OE.411575
Journal © 2020 Received 5 Oct 2020; revised 24 Nov 2020; accepted 5 Dec 2020; published 17 Dec 2020

the subsequent SPDC photon pairs are produced internally in the same waveguide. The cascaded design is simpler and more compact, but requires relatively higher SH power to be generated since the SH is strongest near the end of the waveguide making the subsequent SPDC inefficient. This cascaded interaction in a single periodically-poled lithium-niobate (PPLN) waveguide [8], made by traditional methods of fabrication [9], with SH small-signal normalized conversion efficiency of η<200%/Wcm^2 has been reported [10,11]. In contrast, η>2000%/Wcm^2 have been obtained recently in TFLN waveguides [2,5,12] due to the much smaller mode area in this technology platform; and in turn the higher efficiency leads to higher photon-pair generation rates. A single-waveguide cascaded configuration is convenient because the pump injected into the waveguide can be single-moded, and certain operations, such as producing polarization entanglement from a single-polarization waveguide, become easily realizable [10]. The cascaded configuration in [10] is preferred because it is easier to build a Sagnac loop interferometer if the pump/signal/idler are all in the same wave band. The cascaded configuration is also convenient for other interferometer designs where a pump in the same wavelength-band as the signal and idler can lock the phase of each interferometer [13] for coincidence counting . Furthermore, mode-locked lasers and programmable pulse shapers are commercially available at 1550 nm giving more flexibility and control over the pump [14,15] and in-turn the signal/idler temporal profile.

Recent work on cascading traveling-wave telecom signals in the more efficient TFLN-over-insulator waveguides has been limited to the generation of classical fields. Such work has ranged from cascaded $\chi^{(2)} : \chi^{(2)}$ in TFLN microdisks [16], third-harmonic generation in traveling-waveguides [17], supercontinuum generation [18,19], cascaded SHG/difference-frequency generation for traveling-wave optical parametric amplification (OPA) of both classical signals and quantum noise in waveguides [20], and Raman lasing in resonators [21].

In this work, we expand on our recent findings from [22] where we measure quantum-correlated photon-pairs from a cascaded nonlinear interaction in TFLN at a phase-matching peak with reasonably high quality photon correlations. Our additional studies of noise processes on, close-to and far from phase matching show the effect limiting performance to be Raman scattering from the lithium niobate and we observe a large drop in photon-pair generation when off any phase-matching peak.

2. Correlated photon-pair waveguide source

This TFLN source of correlated photon-pairs is composed of an x-cut 1-cm long waveguide that's poled for a total length of 4-mm (illustrated in Fig. 1) and bonded to Silicon Oxide (SiO_2). The small cross-section of the ridge structure creates a tightly confined transverse-electric (TE) pump and SH mode as predicated by Lumerical simulations in Fig. 1(c) (see [5] for fabrication details). The measured η (see Fig. 2(c)) has multiple phase-matching peaks, the highest around 500%/Wcm^2. The observed η is well above that found in more traditional lithium niobate waveguides such as reverse proton-exchanged waveguides [9], but lags behind the best TFLN devices [5,12]. The multi-peaked phase matching structure are believed to originate from non-uniformities in the poling period of the PPLN.

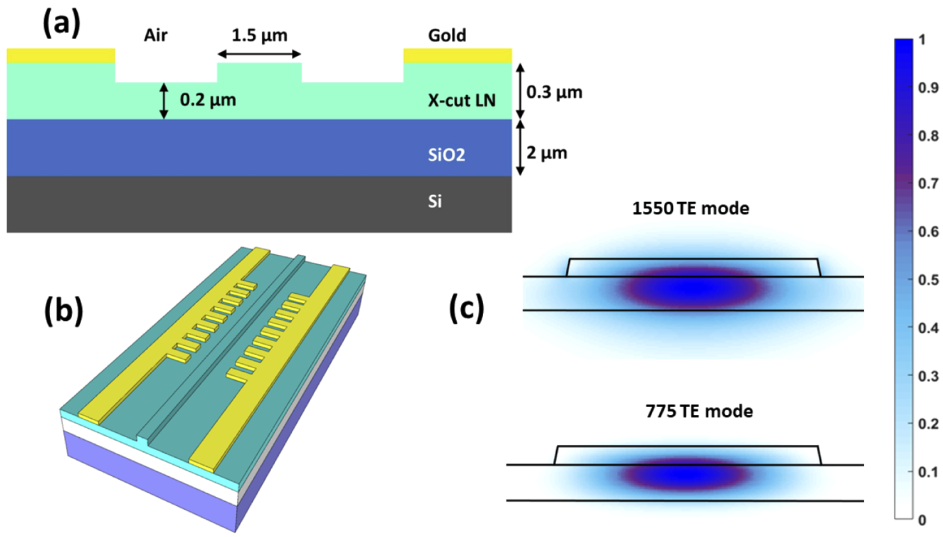

Fig. 1. (a)Waveguide cross-section showing thin 1.5μm wide channel of LiNbO$_3$ (b)Total channel length 1 cm, poled region 4 mm (c)Simulated guided TE modes for 1550 and 775 nm beams from lumerical.

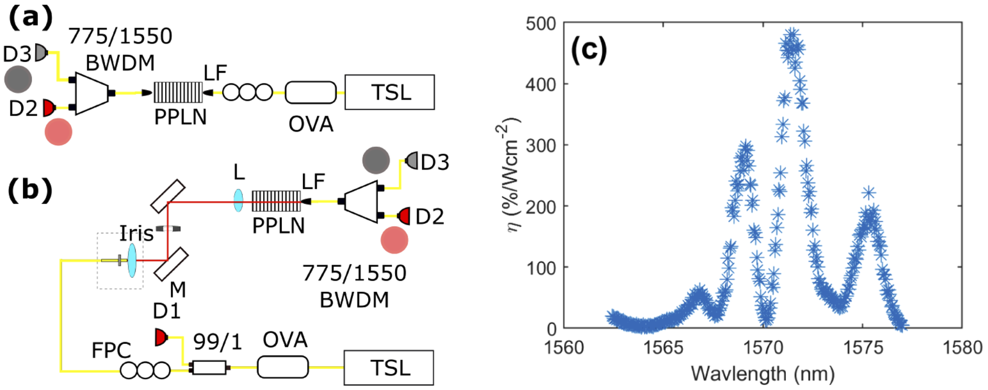

Fig. 2. (a) η measurement setup using CW TSL , OVA (optical variable attenuator), FPC, LF (lensed fiber) for coupling/collecting light to/from PPLN waveguide. 775/1550 BWDM:broadband wavelength multiplexer, D1 & D2 :InGaAs power meter, D2:Silicon power meter, red circle:fundamental band light, gray circle:SH band light. (b) η measurement setup using L:bulk free-space coupling lens for coupling into PPLN. (c) η phase-matching curve taken with (b) and re-scaled to the average value of independent measurements of second highest phase-matching peak.

3. Phase matching and coincidence counting setups

We generate quantum-correlated photon pairs using a cascaded nonlinear interaction consisting of a pulsed fundamental pump at 1569 nm for SHG at 784.5 nm. The SH serves as the pump for SPDC to produce quantum-correlated single/idler photon pairs. The fundamental pump is operated away from the highest main phase-matching peak ($\eta \approx 500\%/\mathrm{Wcm}^2$) because of filter availability. Instead, we operate close to the 2nd highest and distinct peak as depicted in the phase-matching curve of Fig. 2(c) leading to an average η of $270\%/\mathrm{Wcm}^2$ inside the waveguide. The phase-matching curve Fig. 2(c) is measured with two setups from measurements of η defined in Eq. (1). P_F (P_{sh}) are the the measured fundamental (SH) powers exiting the waveguide and G_F (G_{sh}) are waveguide-to-lensed fiber coupling losses for the fundamental (SH). L_{cm} is the total length of all poled regions in the waveguide; the device propagation loss is 1 dB at the fundamental and taken from prior measurements in [23]. The first setup (Fig. 2(a)) couples a continuous wave (CW) pump in/out of the waveguide with lensed fiber (LF) from Oz optics Ltd and is used to determine the waveguide facet-to-lensed fiber coupling loss for the fundamental and SH powers exiting the waveguide. The fundamental and SH facet-to-lensed fiber coupling losses are $G_F \approx 4\,dB$ and $G_{sh} \approx 8\,dB$ with more details discussed in [24]. Figure 2(b) is used in our coincidence counting setup of Fig. 3 with minor alterations, and can be used to calculate the η with CW or estimate the pulsed conversion efficiency per peak point.

$$\eta = \frac{100\% \times G_{sh}P_{sh}}{(G_F P_F L_{cm})^2} \tag{1}$$

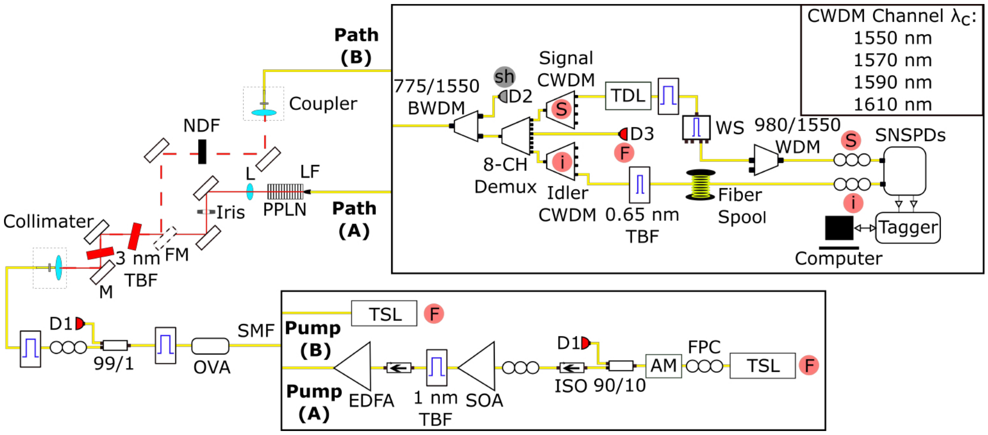

Fig. 3. Channel count measurement system for counts from SPDC and sources of quantum noise with choice of one of two fundamental-pumps: **Pump (A)** and **Pump (B)**, through choice of one of two paths:**Path (A)**, **Path (B)**. **Pump (A)**: Amplified-pulses with nearly 140 ps FWHM at 50 MHz repetition rate. **Pump (B)**:CW TSL. **Path (A)**:Route from the optically pumped waveguide to the quantum-detection system for signal/idler-channel photon pairs. **Path (B)**:Free-space-to fiber bypass of pump to the quantum-detection system of signal/idler-channel photons. TSL:Tunable Semiconducting laser, AM:Amplitude Modulator, 90/10 splitter, D1 and D2:InGaAs power meter (Thorlabs), ISO:fiber isolator, 99/1:99/1% splitter, M:broad band mirror, 3 nm TBF:3 nm Semrock free space tunable filter, FM:flip mirror, L:waveguide-coupling lens, NDF:Neutral density filter, red circle:[fundamental pump (F), signal (S), idler (i)], gray circle:SH, BWDM:broad wavelength division multiplexor, D3:Si power meter (Thorlabs) for SH detection, Demux:8-channel demultiplexer, TDL:time delay line, WS:Finisar 4000s waveshaper

Our pulsed-fundamental pump is formed by modulating CW light from a tunable semiconducting laser (TSL) with an amplitude modulator ran at 50 MHz repetition rate to form ≈ 140 ps FWHM amplified pulses shown in Fig. 4(c). The fundamental-pump pulses are amplified by 2-stages of amplification starting with a semiconducting optical amplifier (SOA), and followed by an erbium-doped fiber amplifier (EDFA). A Newport-1550 1 nm tunable bandpass filter (TBF) is used to reduce saturation at the EDFA; optical isolators are inserted before and after the SOA. The amplified pulsed pump attenuation is controlled by an optical-variable attenuator (OVA) and pre-filtered in two cascaded fiber-coupled TBFs of 1 nm bandwidth. A fiber polarization controller (FPC) is used to excite the low-loss TE mode of the waveguide. The beam is collimated in free space using a fiber-lens collimation package. The collimated beam is filtered by two free-space tunable 3 nm FWHM filters (Semrock) before being coupled into the waveguide with a bulk lens. The fundamental pump out of the EDFA is prefiltered with nearly 210 dB extinction to remove amplified spontaneous emission and fiber-induced Raman scattered light in the signal/idler bands. The fundamental-pump power guided by the PPLN generates SH inside the PPLN that in turn generates photon pairs from SPDC.

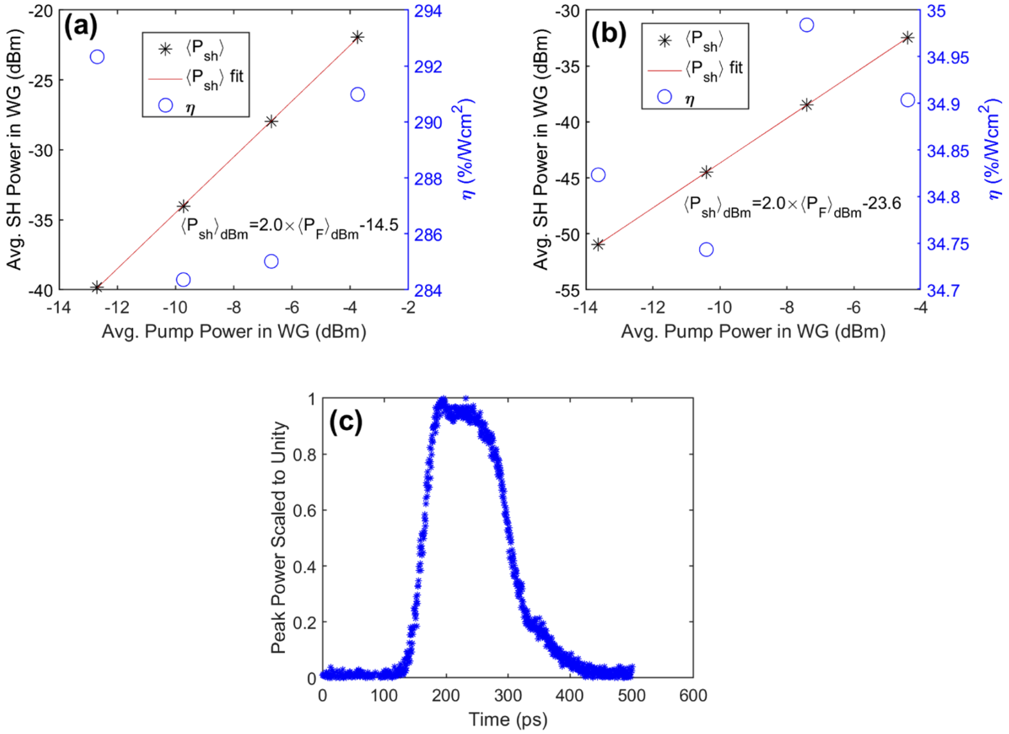

Fig. 4. Average power of pulsed SH (black asterisks) vs average power of fundamental-pump pulse seen inside the waveguide (WG) and the corresponding η (blue circles) calculated from one peak-power point of the fundamental and SH pulses-(see [26] for details)- for (a) pump on a main phase-matching peak at 1569 nm (b) pump off-phase matching at 1566 nm. (c) Measured fundamental-pump pulse shape-see Figs. 6(a) and (b) for corresponding peak powers in Figs. 4(a) and (b).

Proper suppression of both SH and fundamental pumps are crucial for counting quantum photon pairs. The pump, signal, idler are separated by an 8-channel demultiplexer (demux) with 20 nm grid spacing and ≈ 18 nm FWHM Super-Gaussian filters/channel. The SH is separated from pump and signal/idler photon pairs with a custom 775/1550 broad-wavelength division multiplexer (BWDM) from OZ Optics Ltd. Further pump suppression in the idler-channel follows with a 1590 nm coarse wavelength-division multiplexed (CWDM) channel with 18 nm FWHM, and then a TBF with 0.65 nm FWHM. The signal-channel path follows from the demux with a 1550-CWDM, 1 nm Newport 1550 TBF, and Finisar 4000s waveshaper programmed to operate as a bandpass signal filter with 0.65 nm FWHM. The 980/1550 WDM is used to remove photon leakage from the 900 nm internal light source of the waveshaper. The total fundamental-pump (SH) suppression is >210 (150) dB. During photon counting, the waveguide fundamental input/output powers are simultaneously monitored from power meters at the 1% tap at D1 and at D2 through the 1570 nm CWDM channel. The SH is monitored at D3 using a power meter with a silicon detector. Measured optical pulsed and CW sources are given as average powers unless stated other wise; peak powers can be found from [25]. Photons in the signal and idler channels are detected by superconducting nanowire single-photon detectors(SNSPDs) (Opus One by Quantum Opus) with polarization-sensitive detection efficiencies. Photon-detection clicks are time stamped by a Time tagger (Swabian Inc) for time-correlated single-photon counting (TCSPC) and processed by a computer. The polarization-sensitive detection efficiency of each channel was optimized independently by adjusting the photon-polarization state to maximize the singles-count rates per channel. The total loss/channel seen by photons generated inside the waveguide are 18 dB (1550.1 nm signal-channel) and 15.5 dB (1588.4 nm idler-channel) starting from the waveguide-to-lensed fiber coupling interface to detection at the SNSPDs. SNSPD detection efficiency, including FPC and patch-cord losses, was ≈ 70%. The background count rates of our quantum detection system ranged from 610-690 (signal-channel) and 210-270 (idler-channel) due to detector intrinsic dark counts and stray room light leakage into fiberized components of the entire filtering system shown in Fig. 3. The time tagger electrical read-in channels use a dead time of 36 ns that exceeds the 20 ns pulse period of the optical pump applied to the waveguide system. Lost photon counts from detection system dead time is excluded from consideration in all applied loss corrections. Our system is free-running with no gating of the pulsed pump to the time tagger (free-running SNSPDs).

4. Quantum measurement results

4.1. Coincidence generation rate optimization

The coincidence counting measurements are performed with the fundamental-pump set on a phase matching peak at 1569 nm (Fig. 4(a)) and at 1566 nm (intentionally displaced from any of the 3 main phase matching peaks in Fig. 4(b)). Coincidence counting off-phase matching at 1566 nm is performed to diagnose the source of noise in the system since the expected culprit of spontaneous Raman photon generation does not depend on the phase-matching condition. A large drop in the coincidence-count rate is expected when operating off-phase matching at lower η. Pulsed conversion efficiencies (see [26] for details) are ≈ 300 (1569 nm pump) and 35%/Wcm^2 (1566 nm pump) in Figs. 4(a) and (b) over a 10 dB power range that satisfy the undepleted pump approximation for calculating η of Eq. (1). This falls in line with recently reported results [12] on pump-depletion limits in this new TFLN platform when considering both conversion efficiency and fundamental-pump peak powers.

For our pulse-pumped waveguide, we measure the singles-count-rates per channel (SCR), coincidence-count-rates (CCR), and accidental-coincidence-rates (ACR) in our free-running detection system with the coincidence and accidental-coincidences found from computer processed time-tags (see [27]). Unless stated otherwise, all uncertainties for each reported data point are taken from standard deviations of 10 sets of measurements each having 60 s integration times (total time 600 s). Using a pulsed pump (Pump (A) in Fig. 3) through path (A), the channel coincidences are measured and optimized by tuning the idler filter. The idler-filter frequency needed for energy conservation in the SPDC process is $f_i = f_{sh} - f_s$ given the SH-pump frequency (f_{sh}) and signal-channel center frequency (f_s). We tune the idler filter roughly 2 nm around this calculated reference of 1589.4 nm when using a fundamental-pump wavelength of 1569 nm. When the idler filter is tuned ≈ 1 nm away from the peak correlation wavelength the *CCR* closely matches the ACR due to a depletion of correlated signal-idler bandwidth marked by a lack of energy conservation between the measured signal and idler photons. The idler-filter traces out Gaussian-like shapes in Figs. 5(b) and (c) with Gaussian curve fits applied for both the *CCR* and *CAR*. The channel singles-count rate (Fig. 5(a)) remains constant other than negligible variations in loss during filter tuning. The corresponding $CAR = CCR/ACR$ in Fig. 5(c) falls off from a peak at 13.6 ± 0.7 to the theoretical minimum of 1 on both sides of the peak. The average *SCR* (Fig. 5(a)) per channel and *ACR* (Fig. 5(b)) remain constant as expected for the relevant broad-band photon generation processes. The fundamental-pump peak power is set ≈ 40 mW (inside the waveguide) for these measurements.

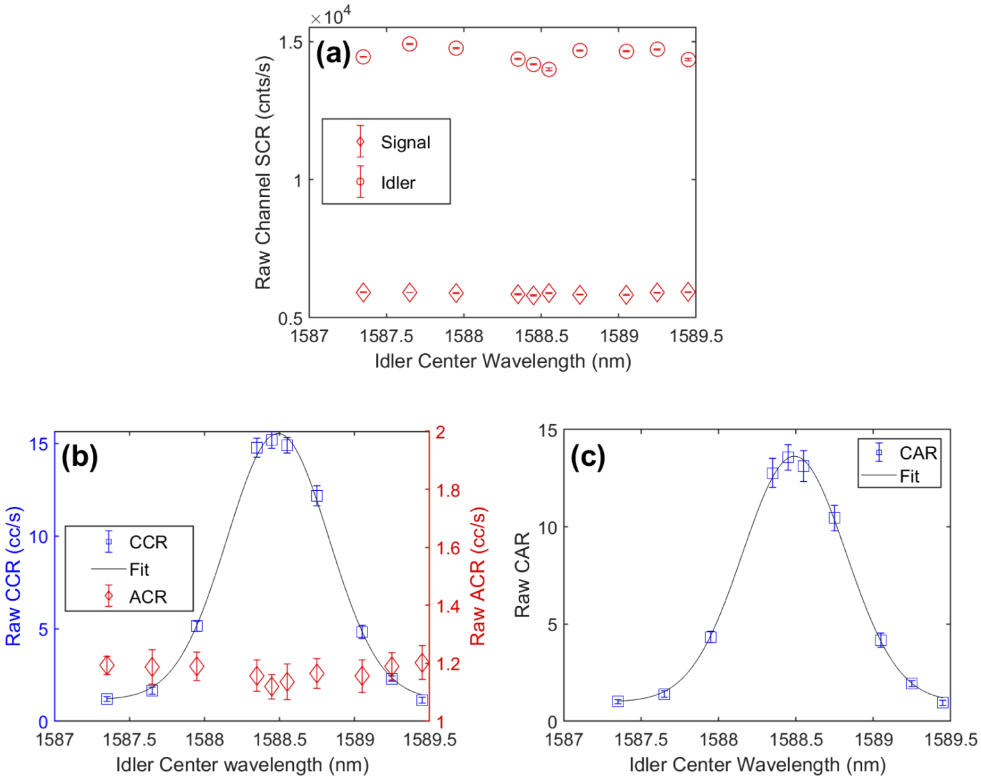

Fig. 5. (a) Measured (raw) singles-count rate (red circles and diamonds) for different idler-filter center wavelengths for the pulsed pump at 1569 nm, and fixed signal-filter at 1550.1 nm and the corresponding (b) *CCR* (blue squares) traced by a Gaussian fit (black line) and *ACR* (red diamonds) showing optimal-correlated and uncorrelated (*CAR = 1*) channels in the *CAR* measurement of (c) where the *CAR* (blue squares) is traced out by a Gaussian fit (black line).

5. Noise analysis

A *CAR* of 13.6 (see Fig. 6(c)) can be used to confirm entanglement of photon-pairs from violation of a Bell inequality between energy & time in a Franson-type setup [28]. A $CAR>6$ corresponds to a visibility $V>0.707$ for two-photon interference fringes (see [29]). However, prior experiments in traditional PPLN have generated CARs well in excess of 1000 [10]. In order to identify the source of noise limiting the observed *CAR*, we perform a series of measurements with the pump both on and off phase-matching using both CW and pulsed excitation. Starting with the pulsed case, we report the power dependence of average *CCR* from photon-pairs, and the average *SCR* per channel. The *SCR* of Figs. 6(a) and (b) for both phase-matching pump wavelengths ($\lambda_{p1} = 1569$ nm and $\lambda_{p2} = 1566$ nm) increase linearly with peak power, and have nearly the same SCR-to-peak power ratio independent of the two η. The η in Fig. 4 differ by nearly a factor of 8, clearly highlighting the noise is a linear pump-system interaction.

We expect the cascaded photon-pair generation rates to be proportional to product of the generated SH-peak power, nonlinear conversion efficiency, and the correlated-frequency bandwidth between closely spaced signal and idler channels [30]. Here, both sets of signal-idler channels are far apart (nearly 40 nm), and the waveguide has a multi-peaked phase-matching curve (see Fig. 2(c)). Both the generated SH power and corresponding *CCR* grow with the square of the fundamental-pump power as shown in Figs. 4(a), (b) and 6(a), (b) for each fundamental-pump wavelength. With a comparative metric called the cascaded-brightness (β)–see Eq. (2)– we compare their respective fundamental-pump peak powers (P_{pk}), generated coincidence-count rates with accidental-coincidences subtracted ($\mathrm{CCR_c}$), and the signal & idler bandwidths ($\Delta\lambda$).

$$\beta \approx \frac{CCR_c}{\Delta\lambda \cdot P_{pk}^2} \tag{2}$$

Ideally, the ratios of the cascaded-brightness β at the two pump wavelengths is expected to differ by nearly the square of their respective η. Instead of the expected factor of 64, we find the β values differ by a factor of 10 for the two pump wavelengths on/off phase-matching [1569, 1566] nm for $P_{pk} = [39.4, 33.8]\, mW$, and $CCR_c = [3.3 \times 10^4, 2.4 \times 10^3]$ cc/s seen inside the waveguide with raw *CAR* [13.3,2.1]. Although further investigation is needed, the close proximity to a SHG phase-matching peak and nonuniform poling may explain the high pair-generation rate at the 1566 nm off-phase-matching operating point.

Overall, the difference in nonlinear conversion efficiency η appears to play no significant role in the SCR/channel. The majority of channel noise is linear with pump power, and can not be attributed to optical parametric amplification of Raman scattered photons. Furthermore, the total fundamental and SH-pump suppression in each signal & idler channel place pump leakage levels below one photon per second when using the maximum system power of nearly 40 mW inside the waveguide. Hence SH and fundamental-pump leakage can be removed from consideration as channel-noise sources.

5.1. Raman noise investigation

Referring to models of Stokes/anti-stokes Raman scattering rates in Eq. (3) from [31], [32] we plot the ratio of the count rates from the signal-channel (I_{as}) to idler-channel (I_s) as $B_{Exp} = I_{as}/I_s$ and compare to $B_{Th} = e^{-hc\Delta\nu/k_bT} \cdot \frac{(\nu+\Delta\nu)^4}{(\nu-\Delta\nu)^4}$ in Fig. 6(d). The parameters h, c, k_b, $T = 300\, K$, $\Delta\nu$, ν, are Plank's constant, the speed of light, Boltzmann's constant, temperature (K), pump frequency shift, and pump center frequency, respectively. Count rates inside the waveguide have dark counts removed before correcting for losses and are measured at fundamental-pump peak powers ranging from nearly 5 to 40 mW. The counts are collected for signal & idler channel-bands each sitting nearly 20 nm from the pump ($\Delta\nu = 77.6$ cm^{-1}). The near equality of B_{Th} and B_{Exp} in Fig. 6(d) shows Eq. (3) is satisfied and the quantum noise source is Stokes/anti-Stokes Raman scattering for both pump wavelengths (1569 and 1566 nm). This Stokes/anti-stokes Raman scattering could originate in either the waveguide or the fiber.

$$I_{as}/I_s = e^{-hc\Delta\nu/k_bT} \cdot \frac{(\nu + \Delta\nu)^4}{(\nu - \Delta\nu)^4} \tag{3}$$

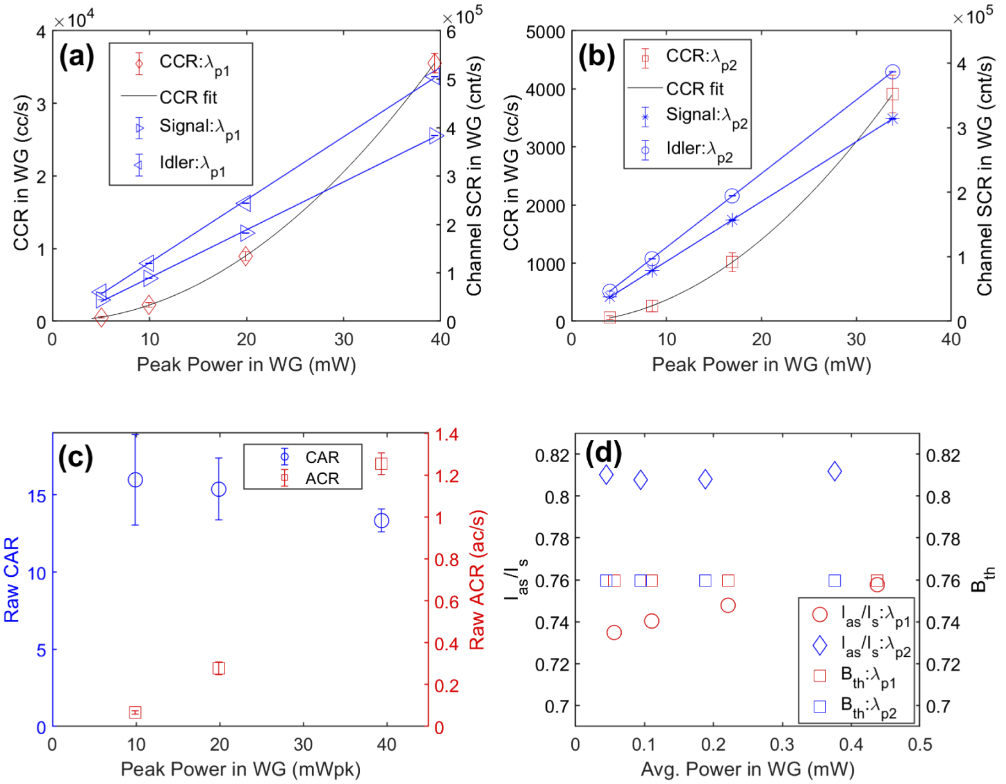

Fig. 6. (a) Generated *SCR* (blue arrows), *CCR* (red diamonds) with quadratic behavior outlined in black for the 1569 nm pumped system. (b) Generated *SCR* (blue diamonds and asterisks) and *CCR* (red squares) with no accidental-coincidence subtraction for the 1566 nm pumped system. (c) Corresponding raw *CAR* and *ACR* for the 1569 nm pumped system omitting *CAR*, *ACR* of lowest power point. (d) Left side of Eq. (3) : Ratio of anti-Stokes/Stokes scattering intensities (red circles) [blue diamonds] for pulsed pump operation point (1569 nm) [1566 nm] compared to the expected Boltzmann statistics Eq. (3) B_{Th} (red squares) [blue squares] of signal & idler channels shifted 77.6 cm^{-1} from the pump operating point (1569 nm), [1566 nm].

5.2. System sources of Raman

We perform a series of measurements using the configuration of Fig. 3 to determine the source of the Raman scattering, which could originate from various sources including the fiber before (after) the waveguide or in either the lithium niobate or SiO$_2$ on the TFLN device. In separate quantum noise measurements, we apply pulsed and CW pumps (Pump (A), (B) of Fig. 3) at both 1566 and 1569 nm. These Stokes Raman scattering rates normalized with respect to pump power inside the waveguide (path (A) of Fig. 3) are plotted in Fig. 7(a) for channels shifted 77.6 cm^{-1} from the pump. The scattering rates/mW-of-pump power inside the waveguide are nearly identical for both pulsed and CW light independent of the η operating points, consistent with spontaneous Raman scattering.

If the dominant contribution to Raman counts originated from pump-fiber interaction before/after the waveguide, then we anticipate a similar count rate can be found when coupling the free-space filtered pump directly into fiber (path (B)) after applying a loss equal the waveguide's insertion loss. With a CW source at 1566 nm we find the scattering rates/mW-of-pump power seen before/after the neutral density filter are $\leq 5\times$ lower than seen inside the waveguide,indicating the

Raman noise is dominated by the waveguide. Our metric of scattering-rate/mW-of-pump power is independent of coupling loss where pump and the idler (shifted 77.6 cm^{-1} from the pump) have the same coupling losses. The free-space-to-fiber system (path (B)) only has one interface for coupling loss that we take to include coupling loss of the collimation package and the series of neutral density filters. In contrast, the measured waveguide insertion loss (in path (A)) is dominated by two interfaces of coupling loss (input and output) where only the output coupling loss is corrected for when stating the pump power. To fairly compare the Raman noise in the two paths for identical frequency shifts using identical input and output pump powers, we list the pump power in the free-space-to-fiber system (path (B)) in Fig. 7(a) using half the insertion loss.

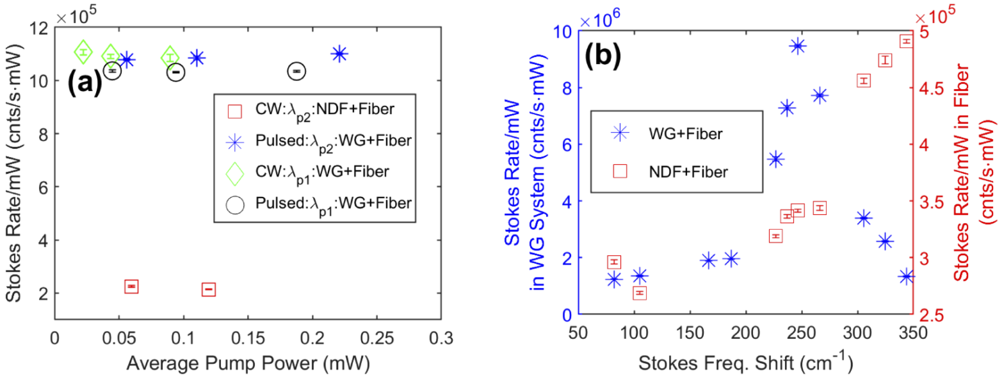

Fig. 7. (a) Stokes scattering-rate/mW-of-pump power generated inside the waveguide (path (A) of Fig. 3) tested separately with CW and pulsed sources. Stokes channels are 77.6 cm^{-1} from both λ_{p1} & λ_{p2} and compared to the scattering rates/mW-of-pump power preceding the NDF of the free-space-to-fiber system (path (B) of Fig. 3). (b) Stoke's spectrum of normalized Raman scattering rates inside the waveguide (path (A)) and the NDF (path (B)).

5.3. *Waveguide material noise source*

The waveguide has two likely sources of Raman scattering, the lithium niobate or the SiO$_2$. To deduce the material scattering source, we take a Raman spectrum of Stokes scattering with offsets up to 85 nm from the fundamental-pump center-wavelength (1530 nm). We use a modified version of Fig. 3 with a CW pump (Santec TSL-210) set at 1530 nm, and free-space filters replaced to give a net isolation ≥210 dB between the pump and idler bands into the waveguide. The 1530 nm operating point is far from phase-matching, and a conversion efficiency could not be assigned for measured second harmonic below the detector noise floor. A spectrum of Raman counts reaching 85 nm from the pump in the idler-channel is measured in the 1550, 1570, 1590, and 1610 CWDMs shown in Fig. 3. The final 0.65 nm TBF is scanned along each CWDM channel to let in Raman photons in this narrower band. The Stokes scattering rates are normalized to the pump power in Fig. 7(b) with the same presentation convention followed for the fiber-to-free space system described for Fig. 7(a). The standard deviation is taken from 5 sets of 60 s measurements (total time 300 s). When going through the waveguide in path (A), the Stokes scattering rate peaks near 250 cm^{-1}. This scattering peak matches closely to the 1st Raman shift in traditional lithium niobate [32] and was seen recently in TFLN devices [21].

Past work in longer lithium-niobate ridge waveguides fabricated with traditional technologies have not been limited by Raman generation in the waveguide. The limiting noise factor is usually Raman in fiber, and CARs > 4000 with $\eta = 16.7\%/Wcm^2$(600%/W) [10] have been reported in PPLN. Our *CAR* is limited by the mismatch between the relatively narrow pump bandwidth and the larger signal/idler bandwidths, smaller net conversion efficiency of our shorter device, and Raman generation from unpoled regions of the lithium-niobate waveguide-channel that do not contribute to true coincidence counts. We can estimate the impact various changes in the experiment would have on *CAR*. Reducing the waveguide length to 4 mm (keeping just the poled region) would reduce Raman counts by a factor of 4/10 and improve *CAR* by about a factor of 6. Given that the transform-limited bandwidth of the 140 ps FWHM pump pulses is <0.03 nm, we could also reduce the filter bandwidth by a factor of 20 (or reduce the pump pulse-width by a factor of 20). The reduced bandwidth would linearly reduce background Raman counts, presuming that the *CAR* is still limited by Raman effects, and these two steps together could improve *CAR* by a factor of 120.

6. Conclusion

In conclusion, we have demonstrated quantum-correlated photon-pair generation in a TFLN platform with *CAR* of 16 ± 2.9. The *CAR* is limited by Raman scattering primarily from $\mathrm{LiNbO_3}$, but this Raman noise can potentially be lowered by shortening the device length to match the total length of the poled regions, and by using a pulse-matched bandwidth for the signal/idler channel bandwidths. However, the *CAR* achieved is already well above the classical limit. The measured coincidence count rates suffer from high losses, and would benefit from integration with on-chip couplers [33], laser dicing, or direct integration of all components on chip to circumvent coupling and insertion losses. We expect the cascaded $\chi^{(2)}$ interaction, which conveniently keeps the pump, signal, and idler in the same waveband, will be useful for future quantum photonic circuits realized in efficient thin-film lithium-niobate waveguides.

Funding

Office of Naval Research (N000141712409).

Disclosures

The authors declare no conflicts of interest in this work

References

1. A. Honardoost, K. Abdelsalam, and S. Fathpour, "Rejuvenating a versatile photonic material: Thin-film lithium niobate," Laser Photonics Rev. **14**(9), 2000088 (2020).
2. J. Y. Chen, Y. M. Sua, Z. H. Ma, C. Tang, Z. Li, and Y. P. Huang, "Efficient parametric frequency conversion in lithium niobate nanophotonic chips," OSA Continuum **2**(10), 2914–2924 (2019).
3. B. S. Elkus, K. Abdelsalam, A. Rao, V. Velev, S. Fathpour, P. Kumar, and G. S. Kanter, "Generation of broadband correlated photon-pairs in short thin-film lithium-niobate waveguides," Opt. Express **27**(26), 38521–38531 (2019).
4. J. Zhao, C. Ma, M. Rüsing, and S. Mookherjea, "High quality entangled photon pair generation in periodically poled thin-film lithium niobate waveguides," Phys. Rev. Lett. **124**(16), 163603 (2020).
5. A. Rao, K. Abdelsalam, T. Sjaardema, A. Honardoost, G. F. Camacho-Gonzalez, and S. Fathpour, "Actively-monitored periodic-poling in thin-film lithium niobate photonic waveguides with ultrahigh nonlinear conversion efficiency of $4600\%\mathrm{W}^{-1}\mathrm{cm}^{-2}$," Opt. Express **27**(18), 25920–25930 (2019).
6. Q. Zhang, H. Takesue, S. W. Nam, C. Langrock, X. Xie, B. Baek, M. M. Fejer, and Y. Yamamoto, "Distribution of time-energy entanglement over 100 km fiber using superconducting single-photon detectors," Opt. Express **16**(8), 5776–5781 (2008).
7. Y. Li, Y. Huang, T. Xiang, Y. Nie, M. Sang, L. Yuan, and X. Chen, "Multiuser time-energy entanglement swapping based on dense wavelength division multiplexed and sum-frequency generation," Phys. Rev. Lett. **123**(25), 250505 (2019).
8. M. Hunault, H. Takesue, O. Tadanaga, Y. Nishida, and M. Asobe, "Generation of time-bin entangled photon pairs by cascaded second-order nonlinearity in a single periodically poled $\mathrm{LiNbO_3}$ waveguide," Opt. Lett. **35**(8), 1239–1241 (2010).
9. K. R. Parameswaran, R. K. Route, J. R. Kurz, R. V. Roussev, M. M. Fejer, and M. Fujimura, "Highly efficient second-harmonic generation in buried waveguides formed by annealed and reverse proton exchange in periodically poled lithium niobate," Opt. Lett. **27**(3), 179–181 (2002).
10. S. Arahira, N. Namekata, T. Kishimoto, H. Yaegashi, and S. Inoue, "Generation of polarization entangled photon pairs at telecommunication wavelength using cascaded χ^2 processes in a periodically poled $\mathrm{LiNbO_3}$ ridge waveguide," Opt. Express **19**(17), 16032–16043 (2011).

11. S. Arahira, N. Namekata, T. Kishimoto, and S. Inoue, “Experimental studies in generation of high-purity photon-pairs using cascaded $X^{(2)}$ processes in a periodically poled $LiNbO_3$ ridge-waveguide device,” J. Opt. Soc. Am. B **29**(3), 434–442 (2012).
12. C. Wang, C. Langrock, A. Marandi, M. Jankowski, M. Zhang, B. Desiatov, M. M. Fejer, and M. Lončar, “Ultrahigh-efficiency wavelength conversion in nanophotonic periodically poled lithium niobate waveguides,” Optica **5**(11), 1438–1441 (2018).
13. S. Wang, C. Chan, P. Moraw, D. Reilly, J. Altepeter, and G. S. Kanter, “High-speed tomography of time-bin-entangled photons using a single-measurement setting,” Phys. Rev. A **86**(4), 042122 (2012).
14. P. Manurkar, N. Jain, P. Kumar, and G. S. Kanter, “Programmable optical waveform reshaping on a picosecond timescale,” Opt. Lett. **42**(5), 951–954 (2017).
15. P. Manurkar, N. Jain, M. Silver, Y.-P. Huang, C. Langrock, M. M. Fejer, P. Kumar, and G. S. Kanter, “Multidimensional mode-separable frequency conversion for high-speed quantum communication,” Optica **3**(12), 1300–1307 (2016).
16. S. Liu, Y. Zheng, and X. Chen, “Cascading second-order nonlinear processes in a lithium niobate-on-insulator microdisk,” Opt. Lett. **42**(18), 3626 (2017).
17. T. Sjaardema, A. Rao, and S. Fathpour, “Third-and fourth-harmonic generation in cascaded periodically-poled lithium niobate ultracompact waveguides on silicon,” in *CLEO: Science and Innovations*, (Optical Society of America, 2019), pp. STh1J–1.
18. M. Yu, B. Desiatov, Y. Okawachi, A. L. Gaeta, and M. Lončar, “Coherent two-octave-spanning supercontinuum generation in lithium-niobate waveguides,” Opt. Lett. **44**(5), 1222–1225 (2019).
19. M. Jankowski, C. Langrock, B. Desiatov, A. Marandi, C. Wang, M. Zhang, C. R. Phillips, M. Lončar, and M. M. Fejer, “Ultrabroadband nonlinear optics in nanophotonic periodically poled lithium niobate waveguides,” Optica **7**(1), 40–46 (2020).
20. Y. M. Sua, J. Y. Chen, and Y. P. Huang, “Ultra-wideband and high-gain parametric amplification in telecom wavelengths with an optimally mode-matched ppln waveguide,” Opt. Lett. **43**(12), 2965–2968 (2018).
21. M. Yu, Y. Okawachi, R. Cheng, C. Wang, M. Zhang, A. L. Gaeta, and M. Lončar, “Raman lasing and soliton mode-locking in lithium niobate microresonators,” Light: Sci. Appl. **9**(1), 1–7 (2020).
22. B. S. Elkus, K. Abdelsalam, S. Fathpour, P. Kumar, and G. S. Kanter, “Quantum-correlated photon-pair generation via cascaded nonlinearity in a thin-film lithium- niobate waveguide,” *Front. Opt. + Laser Sci. APS/DLS* p. LM1F.1 (2020).
23. K. Abdelsalam, T. Li, J. B. Khurgin, and S. Fathpour, “Linear isolators using wavelength conversion,” Optica **7**(3), 209–213 (2020).
24. The waveguide-to-lensed fiber coupling losses of the fundamental and SH can be taken from half the total insertion loss of the waveguide for coupling in/out of the waveguide with lensed fiber at both waveguide facets (excluding lensed fiber insertion losses) of Fig. 2(a). The loss-per-waveguide facet of the fundamental measured in Fig. 2(a) can be found in Figs. 2(b) and 3 if we know the extra loss in the waveguide’s new coupling interface: high numerical aperture bulk lens and fiber-collimation package in Figs. 2(b) and 3. This extra loss is not present in our collection optics using lensed fiber and should not be included in our waveguide’s coupled power or generated photon count rates. We measure this additional coupling loss, remove it, and find good agreement with measured losses from lensed-fiber coupling in Fig. 2(a).
25. Peak powers of the fundamental pump are measured on a fast 40 GHz sampling scope and compared to corresponding measured average powers from a Thorlabs powermeter. This peak-to-average ratio R_f is used to deduce peak powers over the range of average powers measured in each data set.
26. For pulsed sources, η is stated for only one peak point in Fig. 4(c); not for the energy of the entire pulse. We take the fundamental peak-power point and an inferred SH peak-power point -both corrected for all losses starting from the waveguide-to-lensed fiber facet and all fiberized components preceding fundamental and SH detectors. The peak SH pulse power is inferred from the measured average SH power; the expected pulse shape is taken from the square of the measured fundamental pulse in Fig. 4(c). A estimate of the ratio of peak-to-average SH power R_{sh} is taken using the ratio of the fundamental pulse width Δt_f and the inferred SH pulse width Δt_{sh}. The pulsed small-signal normalized conversion efficiency is then approximated as $\frac{P_{sh}\cdot G_{sh} R_f \cdot \Delta t_f / \Delta t_{sh}}{(R_f \cdot G_f \cdot P_f \cdot L_{cm})^2}$, where the Gaussian pulse shape is approximated by square pulses.
27. Accidental count rate (ACR) is inferred from joint detection clicks occurying at channel time delays equal to integer multiples of the pulse period exceeding the measured signal-idler channel time delays. These accidental coincidences are accumulated in an integrated time window of 2 ns.
28. P. G. Kwiat, A. M. Steinberg, and R. Y. Chiao, “High-visibility interference in a bell-inequality experiment for energy and time,” Phys. Rev. A **47**(4), R2472–R2475 (1993).
29. $CAR = CCR_{max}/ACR$ where maximum of CCR is CCR_{max}, and $CCR_{min} = ACR$ for uncorrelated photon-pairs. The visibility $V = \frac{CCR_{max}-CCR_{min}}{CCR_{max}+CCR_{min}} = \frac{CAR-1}{CAR+1} > 0.707$ for $CAR = 13.6$.
30. M. Lobino, G. D. Marshall, C. Xiong, A. S. Clark, D. Bonneau, C. M. Natarajan, M. G. Tanner, R. H. Hadfield, S. N. Dorenbos, T. Zijlstra, V. Zwiller, M. Marangoni, R. Ramponi, M. G. Thompson, B. J. Eggleton, and J. L. O’Brien, “Correlated photon-pair generation in a periodically poled mgo doped stoichiometric lithium tantalate reverse proton exchanged waveguide,” Appl. Phys. Lett. **99**(8), 081110 (2011).

Optics EXPRESS

31. M. Malyj and J. Griffiths, “Stokes/anti-stokes raman vibrational temperatures: reference materials, standard lamps, and spectrophotometric calibrations,” Appl. Spectrosc. **37**(4), 315–333 (1983).
32. S. Zaske, A. Lenhard, and C. Becher, “Efficient frequency downconversion at the single photon level from the red spectral range to the telecommunications c-band,” Opt. Express **19**(13), 12825–12836 (2011).
33. L. He, M. Zhang, A. Shams Ansari, R. Zhu, C. Wang, and M. Lončar, “Low-loss fiber-to-chip interface for lithium niobate photonic integrated circuits,” Opt. Lett. **44**(9), 2314–2317 (2019).